Identification of degree of ordering in spinel LiNi0.5Mn1.5O4 through NMR and Raman spectroscopies supported by theoretical calculations

Gozde Oney, Jon Serrano-Sevillano, Mouna Ben Yahia, Jacob Olchowka, Emmanuelle Suard, François Weill, Arnaud Demortière, Montse Casas-Cabanas, Laurence Croguennec, Dany Carlier

Identification of Degree of Ordering in Spinel $LiNi_{0.5}Mn_{1.5}O_4$ through NMR and Raman Spectroscopies supported by Theoretical Calculations

Gozde Oney[#1,2,3], Jon Serrano Sevillano[#1,4,5], Mouna Ben Yahia[3,6], Jacob Olchowka[1,3,5], Emmanuelle Suard[7], Francois Weill[1,3], Arnaud Demortière[2,3,5], Montse Casas Cabanas[4,5,8], Laurence Croguennec[1,3,5]* and Dany Carlier[1,3,5]*

[1] CNRS, Univ. Bordeaux, Bordeaux INP, ICMCB UMR 5026, F-33600 Pessac, France

[2] Laboratoire de Réactivité et de Chimie des Solides (LRCS), CNRS-UPJV UMR 7314, F-80039 Amiens Cedex 1, France

[3] RS2E, Réseau Français sur le Stockage Electrochimique de l'Energie, FR CNRS 3459, F-80039 Amiens Cedex 1, France

[4] Centro de Investigación Cooperativa de Energías Alternativas (CIC energiGUNE), Basque Research and Technology Alliance (BRTA), Parque Tecnológico de Álava, Albert Einstein 48, 01510 Vitoria-Gasteiz, España.

[5] ALISTORE-ERI European Research Institute, FR CNRS 3104, F-80039 Amiens Cedex 1, France

[6] ICGM, University of Montpellier, CNRS, ENSCM, Montpellier, France

[7] Institut Laue-Langevin (ILL), BP 156, 71 Avenue des Martyrs, 38042 Grenoble, France

[8] Ikerbasque - Basque Foundation for Science, Euskadi Pl., 5, 48009 Bilbao, Spain

[#] equal contributions

Abstract

The performance of the high voltage spinel $LiNi_{0.5}Mn_{1.5}O_4$ (LNMO) in Li-ion batteries strongly depends on its synthesis conditions, actual Ni/Mn stoichiometry, and degree of ordering of Ni and Mn. Depending on the extent of this ordering, the spinel structure can be described in the conventional space group $Fd\bar{3}m$ as the non-substituted $LiMn_2O_4$ or, for the highly ordered phase, in the space group $P4_332$. As previously reported in the literature, using neutron and electron diffraction, a qualitative description of the extent of ordering can be achieved and roughly related to the electrochemical performance of LNMO. To deeper characterize and understand this complex system, in this paper, we will show that Raman spectroscopy, and especially the characteristics of the band located at 160 cm^{-1} attributed for the first time to a twisting motion of octahedral entities, allow to estimate the degree of ordering in LNMO, whereas NMR spectroscopy allows to give a clear description of the local environments of Li, in relationship with the Ni/Mn stoichiometry and extent of ordering. Theoretical calculations were used to support the analysis and attribution of the Raman and NMR signals/spectra. These spectroscopic characterizations enabled in-depth insights into the complexity of LNMO in stoichiometry, degree of ordering, and purity versus the presence of rock-salt or layered oxides as defects or crystalline domains.

Introduction

The spinel, typically described as $LiNi_{0.5}Mn_{1.5}O_4$ or $LiNi_{0.5-x}Mn_{1.5+x}O_4$ (LNMO), is a highly studied positive electrode material for the next generation of lithium-ion batteries owing to its high operating voltage (~ 4.7 V vs. Li^+/Li^0) and specific capacity of 147 $mAh.g^{-1}$.[1–3] Indeed, LNMO positive electrode material possesses a high energy density of 650 Wh/kg, similar to that of $LiNi_{0.6}Mn_{0.2}Co_{0.2}O_2$ (considering a discharge capacity of 170 $mAh.g^{-1}$ and a cut-off voltage of 4.3 V) but with a reduction of 30% of critical elements (Li, Ni, Co) compared to this latter. Two LNMO structures can be obtained depending on the synthesis conditions, differing in composition (mainly in transition metal ratio) and the distribution of Ni and Mn among the transition metals' sites.[4] The disordered LNMO, described in the $Fd\bar{3}m$ space group, is obtained when the transition metal ions are statistically distributed among the 16*d* octahedral sites. In contrast, the ordered LNMO, described in the $P4_332$ space group, is obtained when the Ni^{2+} and Mn^{4+} transition metal ions are localized on the 4*b* and 12*d* octahedral sites, respectively. The disordered LNMO is stabilized when oxygen loss occurs at high temperatures, inducing the formation of Ni-rich rock-salt type impurities, and thus Ni/Mn non-stoichiometry (< 1/3) and partial reduction of Mn^{4+} to Mn^{3+} into the spinel phase for charge compensation.[5–7] Traditionally, the disordered LNMO displays better electrochemical performance than the ordered one due to a higher electrical conductivity. The disorder in the structure allows the delocalization of the electrons between adjacent nickel octahedral sites (Ni^{2+}, Ni^{3+}, and Ni^{4+}), whereas, in the ordered structure, all the Ni^{2+} ions are only surrounded by electrochemically non-active Mn^{4+} ions, thus blocking the delocalization. However, the presence of Mn^{3+} and redox activity of the Mn^{3+}/Mn^{4+} redox couple during extended cycling lead to structural instability, manganese dissolution, and capacity decay, especially in full cells versus graphite due to the cross-talk between the positive and negative electrodes.[8,9]

In fact, a 'degree of ordering' is often observed rather than ideal lattice descriptions.[10–12] The main challenge to successfully bring LNMO to commercialization is understanding the relationship between synthesis conditions, composition, structure and electrochemical properties, to reach optimized performance. An averaged structural information showing differences in the degree of ordering is usually obtained by neutron diffraction[12–15]. The local structure and ordering process are commonly tracked using spectroscopy tools such as ^{6,7}Li solid-state Magic Angle Spinning Nuclear Magnetic Resonance (MAS NMR)[16,17], Raman[18,19] or Fourier Transformed Infra-Red (FTIR).[20,21]

Raman spectroscopy is one of the cost-effective methods for probing LNMO's local environment. Ordering the transition metal ions on distinct sites in the spinel framework results in a lowering of the symmetry from the unit cell described in the cubic space group $Fd\bar{3}m$ (n°227) to the other one described in the cubic space group $P4_332$ (n°212), which increases the expected Raman-active modes from 5 to 40. In a Raman spectrum of LNMO, most of the observed bands in the 350 and 700 cm^{-1} range are assigned to the vibrations of the transition metals and their environments, which allows us to follow their evolution[22,23]. The degree of ordering is roughly qualitatively assessed through the sharpness and larger number of vibration bands for the ordered LNMO compared to the broadening and smaller number of Raman active modes for the disordered LNMO. However, among a series of samples showing the same number of Raman active peaks with similar shapes, the difference can also be finely evaluated through a change in the relative intensity of the first band at ~160 cm^{-1}. This Raman band appears to depend on the degree of ordering [6,24,25], but surprisingly, it is barely identified in the literature for LNMO, and its origin is never discussed.

For paramagnetic materials, the position and shape of the MAS NMR signals depend on the transition metal arrangement around the probed nucleus, here ^{7}Li, and on hyperfine interaction of unpaired electrons of transition metals with the Li s orbitals. The assignment of the NMR peaks to structural environments is not straightforward in paramagnetic materials. The use of DFT calculations to understand the NMR Fermi contact shifts has been proven as a reasonable strategy [26–30]. However, the assignment of the NMR signals in LNMO is still controversial, due to its complex structure. Generally, the degree of ordering is assessed solely based on the number of resonances observed for the sample. If a single resonance is detected, it is attributed to an ordered $P4_332$ structure. Conversely, when a broad NMR signal envelope is detected, it is attributed to a disordered $Fd\bar{3}m$ structure. A previous study by Cabana et al.[31] aimed to attribute observed environments by combining the calculated probability for different Ni/Mn environments for Li, based on neutron diffraction experiments for a prepared LNMO sample, using varying Ni: Mn ratios around the Li atoms from 0 Ni: 12 Mn to 12 Ni : 0 Mn. While commendable as an initial endeavor, their model omitted possible Ni-Mn exchange between the 4*b* and 12*d* sites within the global stoichiometric ratio, nor the presence of Mn^{3+} due to a non-stoichiometry in Li/M or Ni/Mn. Being critical defects for LNMO compounds depending on the synthesis conditions, these hypotheses merit consideration to support this study and others to come.

A precise comprehension of the ordering process within the spinel structure of LNMO remains elusive due to its intimate relationship with the synthesis conditions, which depends on the thermal treatment (temperature, duration, atmosphere, among others …) but also on the Li:Ni:Mn stoichiometry within the pristine precursor mixture. It explains why the degree and origin of ordering remain controversial in the scientific community, which is still seeking a deeper understanding and, thus, the support of adapted characterization tools.

In this paper, we combined theoretical DFT calculations with experimental NMR and Raman spectroscopy characterizations of highly disordered and highly ordered LNMO samples to provide a full comprehension of the observed spectra. This contribution is expected to substantially aid in acquiring valuable information regarding the fundamental mechanisms steering the ordering phenomenon.

Experimental Method

1. Material Synthesis

The LNMO samples were prepared by molten salt synthesis, as described in detail in our previous work.[32] Stoichiometric amounts of $Ni(NO_3)_2 \cdot 6H_2O$ and $Mn(NO_3)_2 \cdot 4H_2O$ (1:3) were mixed with an excess amount of LiCl salt (with a ratio of 35 for number of moles of LiCl/number of moles of transition metals) to obtain 1g of LNMO. All powders were provided by Sigma-Aldrich (> 97,0 %). The powder mixture was calcinated at 750°C for 4 hours in a tubular furnace in an alumina boat under an air atmosphere. The heating ramp was at a rate of 3°C per minute, while the cooling ramp was at 1°C per minute. The excess of LiCl was first washed using distilled water and then several times with ethanol to successfully clean any residual salt at the material's surface. The obtained compound was named "*d*-LNMO" for disordered LNMO, whose structure is described in the $Fd\bar{3}m$ space group with a random distribution of the transition metal ions within a single octahedral crystallographic site. An additional annealing step was performed under continuous O_2 flow at 700°C for 24 hours to order the transition metals, the nickel ions occupying one octahedral site and the manganese ions at another octahedral site (4*b* and 12*d* sites, respectively, in $P4_332$ space group). This annealing step was repeated a second time with a grinding step in between to homogenize the material. The heating ramp was kept the same as for the first annealing, while the cooling ramp was increased to 2°C per minute. The obtained re-annealed LNMO powder was labeled "*o*-

LNMO" for ordered LNMO, whose structure is described in the $P4_332$ space group, as seen in the neutron diffraction pattern in **Figure 1a**.

2. Material characterization

Powder X-ray diffraction (XRD) measurements were carried out with a PANalytical Empyrean Diffractometer with Cu $K\alpha_{1,2}$ radiations in a Bragg-Brentano configuration. Diffraction patterns were collected in a 2ϑ range of 15-120°(2ϑ) with a scan step of 0.008° for a total acquisition of 20 hours. The room temperature neutron powder diffraction (NPD) data were measured on the D2B high-resolution diffractometer of the Institute Laue-Langevin (ILL) in Grenoble, France (transmission geometry with a wavelength of 1.594 Å) in the 2θ angular range of 0-160° with 0.05° 2θ-steps during a total accumulation time of 4h per pattern. The structural parameters were determined using the FullProf program[33] via Le Bail and Rietveld refinements.

To determine the composition in Li, Ni, and Mn, elemental analyses by inductively coupled plasma-optical emission spectroscopy (ICP-OES) were performed using Agilent 5800 spectrometer after complete dissolution of the sample in an equal volumic mixture of hydrochloric (HCl) and nitric (HNO_3) acids. The Li:Ni:Mn ratios were found to be in good agreement with those expected 1:0.5:1.5, as reported in **Table S1** in supplementary information.

The electron diffraction patterns were collected using the selected area technique (SAED) on a microscope JEOL JEM-2100 (LaB_6) at 200 kV with an Orius 200D (Gatan) camera. The LNMO powder was dispersed in EtOH and deposited on a copper TEM grid.

The Raman spectra were acquired using a confocal LabRAM HR Evolution micro-spectrometer (Horiba) using a 633 nm Argon gas laser source and a 600 gr/mm grating. Each spectrum was collected from 100 to 800 cm^{-1} using a 10.6 mm focal length lens, with an acquisition time of 10 s and 40 accumulations. All the data were normalized to the intensity of the peak at 500 cm^{-1}, as the oxidation state remains constant for Ni between samples (i.e., Ni(II)).

^{7}Li solid-state MAS NMR experiments were performed on a Bruker Avance III 100 MHz (2.35 T) spectrometer with a 2.5 mm MAS probe. A rotor-synchronized Hahn echo ($\pi/2-\pi$) sequence was used with a $\pi/2$ pulse length of 1.1 µs and a recycle delay of 0.2 s. 96000 scans were acquired. The spectra were referenced to a 1 M solution of LiCl. All samples were prepared under air, and spinning frequencies were set to 30 kHz. The spectra were fitted using the Dmfit software.[34]

3. Electrochemical characterization

The positive electrodes were prepared by mixing 80:10:10 wt.% of synthesized LNMO powder, carbon black conductive additive (Alfa Aesar, 99.9%), and Poly(vinylidene fluoride) (PVDF, Sigma-Aldrich) binder in 1-methyl-2-pyrrolidone (NMP, Sigma Aldrich, 99.5%) for 3 hours under stirring, and then the obtained slurry was cast on Al foil. The prepared positive electrodes were assembled in CR2032-type coin cells using Li metal as the negative electrode and a Whatman® separator impregnated with the 1M $LiPF_6$ EC/DMC electrolyte (1:1 w/w ethylene carbonate (EC) / dimethyl carbonate (DMC)). The electrode loading for all samples was around ~3 mg/cm^2 of LNMO active material.

4. Computational Details

Simulation of Raman spectra - To investigate the vibrational properties of LNMO ordered structure, the B3LYP density functional method, well-known for its ability to reproduce this type of property and a spin-polarized all-electron description, was employed.[22,35–39] Calculations were performed on relaxed structures within the harmonic approximation using the CRYSTAL17 code.[40] The Raman intensities were determined using the analytical Coupled Perturbed Kohn-Sham (CPKS) method.[41,42] High-density k-mesh was employed as well as large Gaussian-type basis sets:[22,40–43] 6-11 for Li, 86-411 (d41) for Mn, 86-411 (d41) for Ni, and 8-411 for O[38,43], respectively to ensure the convergence of the optical properties.

Simulation of NMR shifts - Different crystal structures were fully relaxed with the Vienna ab initio Simulation Package (VASP).[44,45] Spin-polarized DFT calculations were performed, and projector-augmented wave potentials[45] were used to replace core electrons, whereas Li (2s), Mn (3p, 3d, 4s), Ni (3p, 3d, 4s) and O (2s, 2p) valence electrons were expanded in plane-waves with a cut-off energy of 600 eV. The Perdew-Burke-Ernzerhof (PBE)[46] exchange-correlation function was used with a Monkhorst-Pack grid. Atomic positions and unit cell were relaxed with a residual force threshold of 0.02 eV.Å^{-1}. The generalized gradient approximation with the Hubbard parameter correction (GGA+U) of Dudarev et al.[47] was employed with a U value of 3.9 and 6.2 for Mn and Ni, respectively, and a k-mesh dense enough to reach the convergence. The chemical shifts were calculated as in previous reports.[27,48–50] The NMR signals were simulated using a Gaussian function with the “numpy” and “peakutils” libraries in Python. The peak position was obtained from the computed chemical shift. The amplitude was obtained from the amount of environments corresponding to the defined shift position. The peak width was adjusted to resemble the *d*-LNMO experimental line broadening with a FWHM of around 50 ppm.

Results and discussion

The two prepared LNMO samples will be carefully characterized and compared in the following, combining solid-state NMR and Raman spectroscopies as well as theoretical calculations to support the in-depth characterization of these spectroscopic data. However, it is first imperative to establish a comprehensive understanding of the two samples: *o*-LNMO, which exhibits a high degree of ordering of transition metals, and *d*-LNMO, characterized by a high transition metal disorder.

Their XRD patterns, given in **Figure S1** in the supplementary information, reveal the formation of single spinel-type phases without impurities such as NiO-type rock-salt, which is not common for the disordered spinel as reported recently in previous work[32], but essential for in-depth characterization of the degree of ordering. Their lattice parameters are 8.1759(2) Å and 8.1679(4) Å for *d*-LNMO and *o*-LNMO, respectively. This decrease of parameter with the transition metal ordering is consistent with previously reported data in the literature and is due to the oxidation of Mn^{3+} into Mn^{4+} during the second annealing step, as their ionic radii are 0.785 Å for Mn^{3+} and only 0.67 Å for Mn^{4+} [51,52].

Neutron powder diffraction (NPD) was used to obtain an average description of the cationic ordering, as the difference in neutron scattering lengths between Ni and Mn atoms (b_{Mn} = -3.73 fm and b_{Ni} = 10.3 fm, respectively[53]) enables differentiation of their positions. Indeed, while the XRD patterns in **Figure S1** suggest that the two phases are very similar, the corresponding NPD patterns reveal a clear difference in the number of diffraction peaks observed for *d*-LNMO and *o*-LNMO, as highlighted in **Figure 1a**. For *o*-LNMO, the presence of reflections with "h", "k" and "l" of different parity (violating the reflection condition for the F-centered lattice), such as (110), (210) and (211), indicates a lowering of the symmetry from $Fd\bar{3}m$ to $P4_332$ due to an ordered distribution of Ni and Mn within the structure in two different octahedral sites.[13]

Several hypotheses of defects were evaluated in these spinel-type phases by refining their neutron diffraction patterns with the Rietveld method, including a possible non-stoichiometry in Ni/Mn in both samples, cation mixing on the two octahedral sites of *o*-LNMO, and exchange between the tetrahedral and octahedral sites of *o*- and *d*-LNMO. Initially, the sites' occupancies of Li and O atoms were assessed, and this indicated a tendency toward full occupation of sites, which agreed with the theoretical description. Then, the stoichiometry in Ni/Mn was checked. For *d*-LNMO, a 2.5% of Mn over-stoichiometry was revealed (**Figure S2 and Table S2**), while

for *o*-LNMO, it decreased to 0.5%. The chemical formula of the spinel phase can thus be written as $LiNi^{II}_{0.461}Mn^{III,IV}_{1.539}O_4$ for *d*-LNMO, with 5% of Mn^{3+}, and $LiNi^{II}_{0.492}Mn^{III,IV}_{1.508}O_4$ for *o*-LNMO, with less than 1% Mn^{3+}. Furthermore, despite similar compositions in Ni and Mn for the two samples *o*- and *d*-LNMO and, as just discussed, different stoichiometries in transition metals for the spinel phases they contain, no secondary phase was identified by XRD and NPD. Nevertheless, despite not being observed, most probably due to too small coherent domain size for diffraction, Ni-rich domains should exist for composition compensation. Note that the cation-mixing model was found invalid for *o*-LNMO due to negative occupancies for Mn in the 4*b* site and Ni in the 12*d* site. Similarly, no Li/Mn exchange was identified for *o*- and *d*-LNMO between tetrahedral and octahedral sites. However, a small exchange was found to be possible between Li in the tetrahedral site and Ni in the octahedral site: only 0.2% for *d*-LNMO (**Table S2**) and 1.2% for *o*-LNMO, with similar results and reliability factors to those obtained for the fully ordered spinel structure (**Figure S3, Table S3**). Even though neutron diffraction provides insight into the general composition of the spinel-type phases, it remains an average structural description. Insight from spectroscopies is clearly required to get local information, confirm any possible Li/Ni exchange for *o*-LNMO, and especially describe the distribution of Ni/Mn among the octahedral sites of *d*-LNMO. Indeed, in the $Fd\bar{3}m$ unit cell, Ni and Mn atoms occupy the same crystallographic site.

As shown in **Figure S4,** selected area electron diffraction (SAED) patterns support the homogeneity of the samples at the LNMO primary particle level. Indeed, all diffraction patterns collected for *o*-LNMO showed additional diffraction spots along the zone axis that permit the distinction of the two structures, in agreement with the local ordering of Ni and Mn within the transition metal network. In contrast, their absence in all diffraction patterns collected for *d*-LNMO confirmed the transition metal disorder.

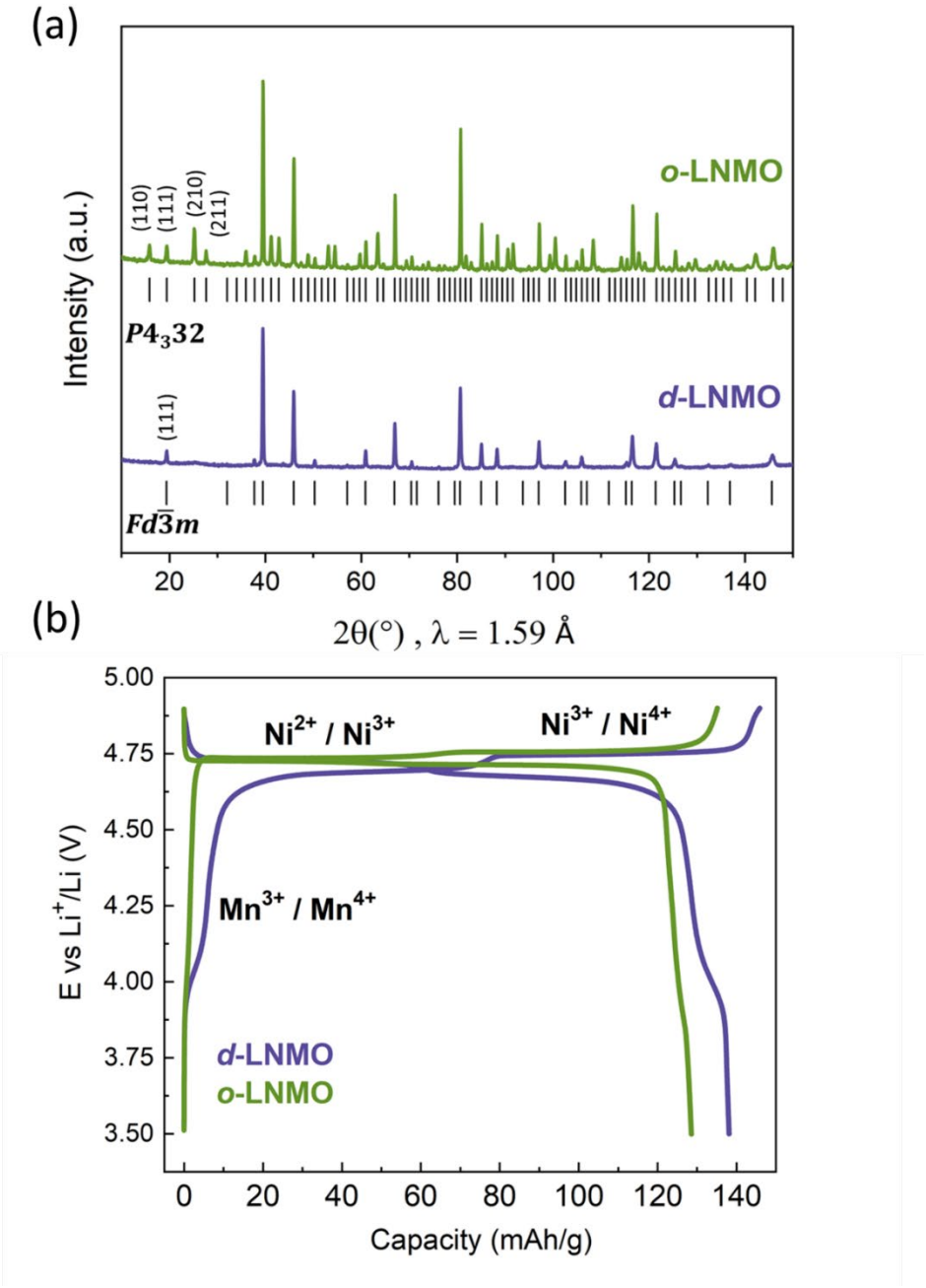

Figure 1: (a) Comparison of powder neutron diffraction patterns of *d*-LNMO and *o*-LNMO samples. (b) Second cycle charge-discharge galvanostatic curves at C/10 cycling rate.

Figure 1b compares the second charge/discharge curves of both LNMO materials at a cycling rate of C/10 (10 hours for one theoretical Li^+ exchange), this one being representative of actual Li^+ (de-)intercalation from the active material while the first cycle is also affected by electrolyte degradation at high voltage and associated to the formation of the cathode-electrolyte interface (CEI). For the sample *d*-LNMO, a reversible electrochemical activity is observed at around 4.0

V *vs.* Li^+/Li, corresponding to the Mn^{3+}/Mn^{4+} redox couple. This contribution has almost vanished for the sample *o*-LNMO, as expected, considering its synthesis conditions and structural description discussed in detail just before. The contribution of the Mn redox activity to the global capacity is estimated by the analysis of the dQ/dV plots given in **Figure S5** to be 4% for the sample *d*-LNMO, while it decreases to 1% for *o*-LNMO, in agreement with the Mn^{3+} content estimated by the neutron diffraction analysis. Concerning the Ni redox, two different mechanisms were observed depending on the cation distribution within the transition metal network, either ordered or disordered, as reported in the literature[4]. The sample *d*-LNMO is characterized by an electrochemical curve with two distinct activities (one pseudo-plateau and a plateau) at 4.69 V and 4.75 V *vs.* Li^+/Li, corresponding to a solid-solution reaction involving the Ni^{2+}/Ni^{3+} redox couple and to a biphasic reaction involving the Ni^{3+}/Ni^{4+} redox couple, respectively. In contrast, for *o*-LNMO, two consecutive biphasic plateaus were observed at rather similar voltages, *i.e.,* 4.74 and 4.76 V *vs.* Li^+/Li ($Ni^{2+}/Ni^{3+}/Ni^{4+}$ redox couples). The discharge capacity is higher for the sample *d*-LNMO than for the sample *o*-LNMO, 138 $mAh.g^{-1}$ vs. 128 $mAh.g^{-1}$, respectively. This higher capacity observed for disordered material agrees with previous studies that have been reported.[54,55]

Insights of Raman Spectroscopy on Transition Metal Order and Possible Defects

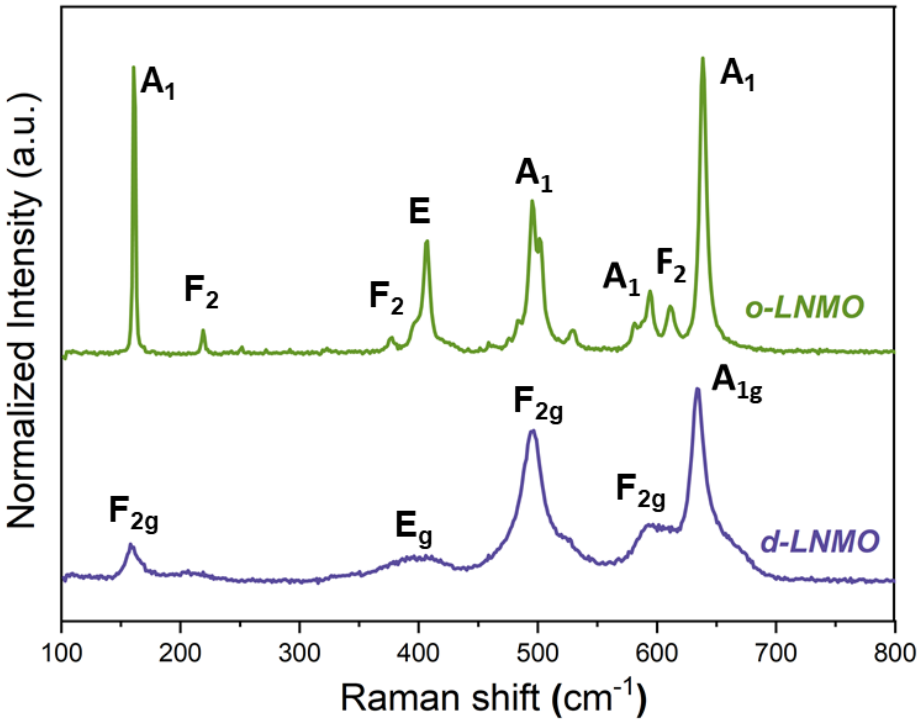

Figure 2: Raman spectra of prepared LNMO samples. The intensity was normalized based on the peak observed at ~500 cm^{-1}, sensitive to the Ni oxidation state and its coordination (here unchanged, as there is only Ni^{2+}).

Raman spectroscopy is one of the most widely used techniques for evaluating the degree of transition metal ordering within the spinel system. Because of the change in lattice symmetry between the two structures, there is a great difference expected both in the Raman bands' width and in the number of Raman active modes predicted from group theory applied to the ideal structure: $A_{1g} + E_g + 3F_2g$ active modes for disordered spinel ($Fd\bar{3}m$ s.g.) vs. $6A_1 + 14E + 20$ F_2 for ordered spinel ($P4_332$ s.g.). **Figure 2** compares Raman spectra collected for the two LNMO samples. For *d*-LNMO, a spectrum with seven distinguishable broad peaks at 160, 400, 495, 525, 590, 635, and 655 cm^{-1} is observed, consistent with the formation of a disordered spinel phase [55,56]. The reason behind the increased number of observed Raman bands (7) in comparison to the predicted ones (5) primarily arises from the presence of different cations (Ni^{2+}, $Mn^{3+,}$ and Mn^{4+}) occupying the same site, leading to distinct MO_6^{n-} local environments, which is not predicted for the ideal structure. In contrast, for *o*-LNMO, a highly resolved spectrum with many active modes and a significantly greater overall intensity is obtained. The

40 expected vibrations are, most of the time, experimentally not all observed for an ordered spinel phase. This can be attributed to certain modes having activities close to zero, as well as to imperfect transition metal ordering and experimental resolution limitations. Our *o*-LNMO exhibits one of the highest resolved spectra ever reported to date, with multiple sharp peaks of small intensity that can be clearly distinguished from the baseline, indicative of a locally high degree of ordering (**Figure S6**). Moreover, the sharpness of the bands reaching the experimental value with FWHM (full width at half maximum) of 3 cm^{-1} **(Figure S7)** confirms the high resolution and, consequently, the high ordering in the system.

Most of the observed peaks in the spectra can be attributed to their corresponding vibration modes, thanks to both previous experimental and theoretical work on the spinel structure[22,23,56] and this work. At higher wavenumbers, nucleus-focused vibrations can be observed, providing information about the metal coordination environment. **Figure S7** presents the decomposition of the obtained spectra for both samples, and **Table S4** shows their attribution. The intense peak observed for *d*-LNMO, around 635 cm^{-1}, has A_{1g} symmetry and is primarily associated with the stretching of Li-O bonds, particularly involving the displacement of oxygen atoms bonded to Mn ions, which leads to the breathing of the MnO_6 octahedron[22]. Thus, its frequency is sensitive to the degree of oxidation of the Mn atoms. Similarly, the intensity of the shoulder observed at 655 cm^{-1} is influenced by the concentration of Mn^{3+} exhibiting a local Jahn-Teller (JT) type distortion. The shift to higher wavenumbers results from local distance disparities, and the intensity is proportional to JT Mn^{3+} concentration as polarizability is extensive.[57] This shoulder observed at 655 cm^{-1} for the *d*-LNMO sample disappears for the *o*-LNMO sample that has undergone the second annealing at 700°C, confirming thus the oxidation of Mn^{3+} into Mn^{4+} during this thermal treatment.

Between 550 and 700 cm^{-1}, a splitting of the F_{2g} modes is observed when the spinel-type material is ordered, indicating a lowering of the lattice symmetry. The peaks around 400 and 495 cm^{-1} also originate from vibrations of the Li-O bonds, but this time, the oxygen atoms are predominantly connected to nickel. Thereby, these two bands are mainly sensitive to the oxidation state of the Ni atom.[22]

Additional information about the organization at a longer range can be obtained at low wavenumbers associated with lattice vibrations in Raman spectroscopy. For instance, despite being rarely commented on, the Raman spectra are often not reported with a Raman shift below 200 cm^{-1}; the drastic change in intensity observed on the peak at 160 cm^{-1} is a good indicator of the degree of ordering. The higher the intensity for this peak, the more ordered the spinel phase

is. However, its origin was never precisely explained. This type of low wavenumber mode is also observed for phases such as Co_3O_4[58], $NiCo_2O_4$[59], and $NiFe_2O_4$[60,61] spinels, and it was tentatively attributed to the presence of a highly polarizable divalent metal, such as Co(II), Ni(II) and Fe(II) in tetrahedral sites. Intending to understand the origin and changes in the intensity of this vibration band and verify the effects of possible defects on the experimental spectra, we thus conducted DFT calculations on the ideal and defective lattices of the $P4_332$ structure.

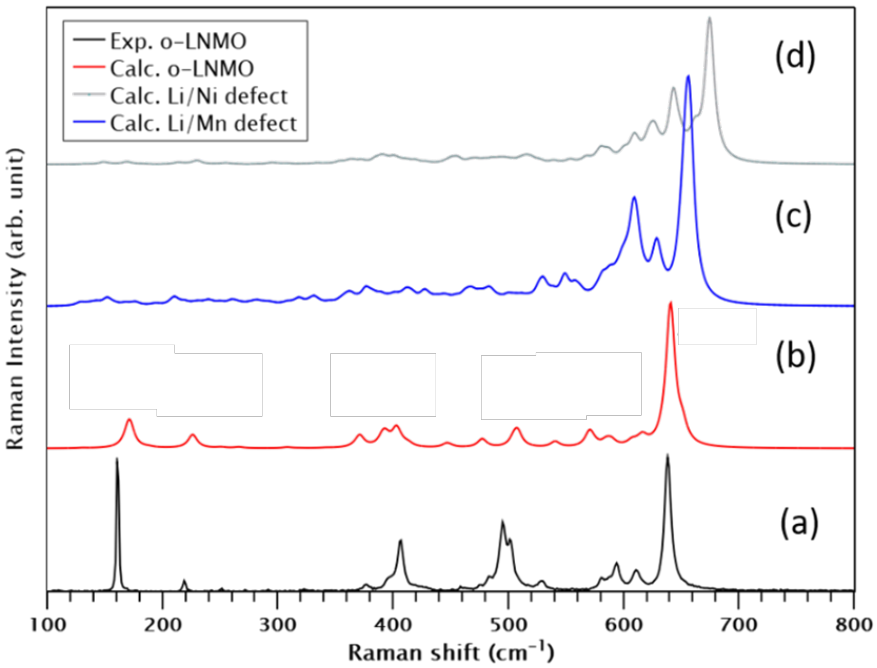

Figure 3: The experimental Raman spectrum of the *o*-LNMO sample (a) was compared to different calculated spectra: the defect-free spectrum (b), the hypothetical models considering Li/Mn (c) and Li/Ni (d) antisite defects. These models are assumed at an exchange rate of 0.125. A scaling factor of 0.96 was applied to the wavenumbers[62], and a classical half-value Lorentzian width of 5 cm^{-1} was used to accurately reproduce the intensities of each normal mode.

Figure 3 compares the experimental Raman spectrum and the spectrum calculated for the ideally ordered $P4_332$ structure. It reveals a rather good agreement between both, especially in the positions of the different peaks and more roughly in their intensities: indeed, some are underestimated.

As mentioned, we are mainly interested in the low-frequency peak at ~160 cm^{-1} and the effect of possible defects on its position and intensity. Based on our calculations, it contains two

distinct normal modes involving the participation of lithium and oxygen atoms, with a different contribution from the second coordination sphere (*i.e.,* the transition metals). The first mode with A_1 symmetry and positioned at 171 cm^{-1} (from theoretical calculations) corresponds to a twisting motion of octahedral entities, on average, for 3 Mn **(Video S1)**. The second threefold degenerated F_2 mode, located at 166 cm^{-1} involves a twisting and gliding motion in the three directions of the space of entities comprising 3Mn and 1Ni with a major participation of the latter **(Video S2).** The A_1 mode exhibits the highest intensity, while the intensity of the F_2 mode is almost negligible (relative activity is about 28 times greater).

To better understand the origin of this peak, different models with local defects were explored: *(i)* First, with a Li/Ni or Li/Mn exchange between transition metal atoms in octahedral sites (4*b* or 12*d*) and lithium atoms in tetrahedral sites (8*c*), then *(ii)* with a Mn/Ni exchange between the octahedral sites of transition metals (12*d* and 4*b*). More details are given on these models in the supplementary information, and **Table S5** compares especially their stability versus that of the fully ordered spinel-type structure.

Li/Mn and Li/Ni antisite defects reveal more noticeable alterations in the 600-700 cm^{-1} region than in the low-frequency region (**Figure 3c-d**). First, as highlighted by the comparison of free energy versus that of the perfectly ordered spinel *o*-LNMO in **Table S5**, the exchange between Td/Oh sites is unexpected as it shows lower thermodynamic stability than the reference ordered model. Then, the wave numbers corresponding to the hard modes, specifically those above 500 cm^{-1}, are blue-shifted by 25-70 cm^{-1}. Notably, the most prominent mode within the ordered *o*-LNMO phase, which is initially calculated at 640 cm^{-1}, is shifted approximately by 35 cm^{-1} (**Table S6**). This variation is mainly attributed to the shortening of some M-O distances versus those observed for the *o*-LNMO reference phase. The absence of predicted frequency shift and intensity increase for antisite Td/Oh defects in the experimental spectra refutes further major Li/Ni or Li/Mn exchange in the highly ordered phase. This agrees with neutron diffraction analysis on the *o*-LNMO sample, as no Li/Mn exchange was observed, and only limited Li/Ni with less than 1.2% was found plausible. Besides, as highlighted in **Figure S8**, the Ni/Mn (Oh/Oh) exchange is also not observed in the ordered $P4_332$ sample.

Finally, all the considered models were found to be less stable than the fully ordered structure for the stoichiometric composition $LiNi_{0.5}Mn_{1.5}O_4$, and they always predicted a lower intensity for the Raman mode at 160 cm^{-1}. However, even with the stoichiometric consideration, the theoretical calculations are limited in replicating this intense and sharp peak. The functional used for the calculations may be exaggerating the polarizability of the M-O bonds, thus

increasing the relative intensity of the high-frequency bands, mitigating the overall intensity on the low-frequency region. Additionally, numerous studies have demonstrated that the FWHM of a mode is inversely proportional to the phonon's lifetime.[63–66] This latter is maximal for a perfect crystal, whereas it becomes shorter when the coherent domain size decreases, as limited when phonons encounter defects. Consequently, we can hypothesize that an increased coherent ordered domain size (calculated as 45 nm for the *o*-LNMO from NPD data as discussed earlier) can lead to a sharp vibration band at 160 cm^{-1} (The FWHM decreases to 3 cm^{-1} experimentally) while rising its intensity. Note that the larger peak shape at ~160 cm^{-1} observed for *d*-LNMO (**Figure 2**) is, as expected, in good agreement with the existence of a large number of defects, small coherence length, and thus limited phonons' lifetime. It is important to point out that in this case, the presence of different cations (e.g., Ni^{2+}, Mn^{3+}, and Mn^{4+}) on the same crystallographic site is perceived as a defect, reducing phonon's lifetime. Finally, our results have shown that the origin of the high intensity and sharp band at 160 cm^{-1} comes from large, highly ordered domains and not from antisite defects in the structure.

Insights of Nuclear Magnetic Resonance Spectroscopy on Transition Metal Order and Local Li Environments

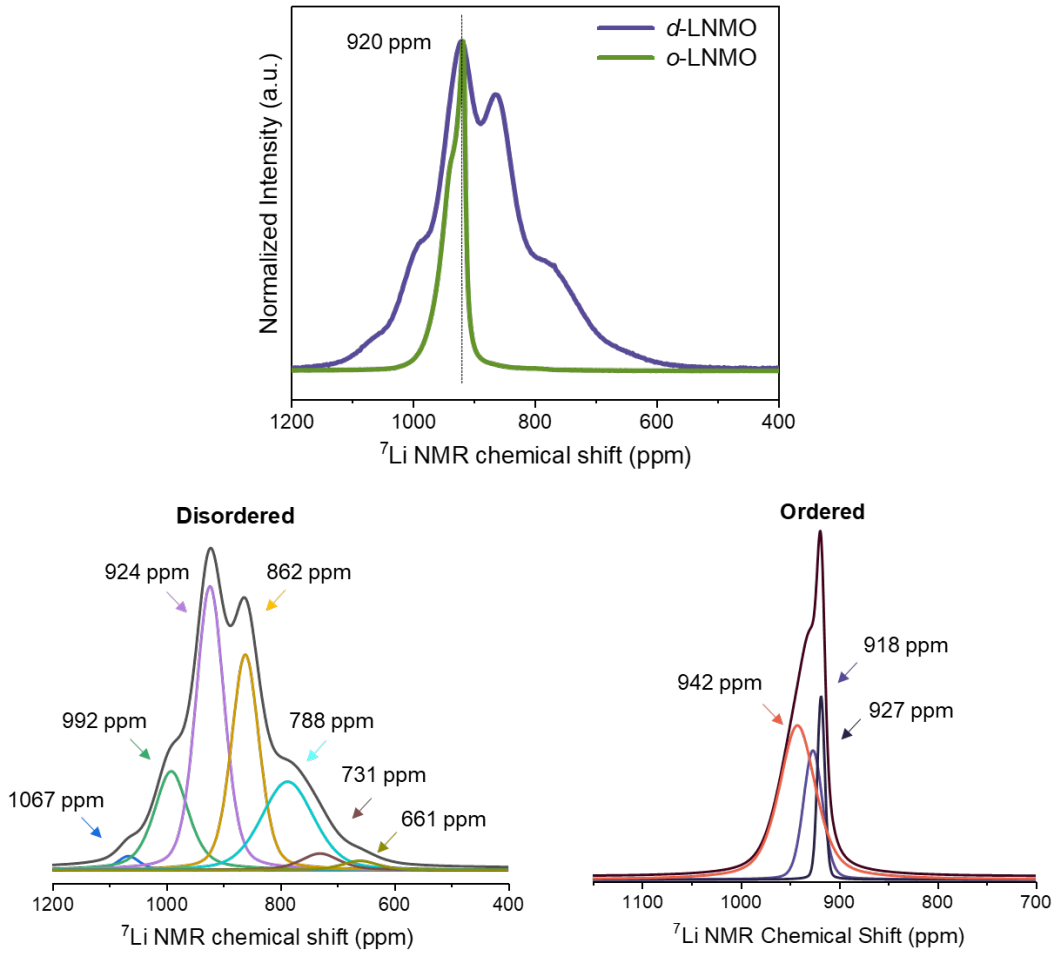

Figure 4: ^{7}Li solid-state MAS NMR spectra and their decomposition for *d*-LNMO and *o*-LNMO phases.

^{7}Li solid-state MAS NMR is a useful tool for getting local information on transition metal organization in spinel structure because of its high sensitivity to changes in the coordination shells around Li atoms. It thus allows the degree of ordering to be evaluated.[67] **Figure 4** compares the ^{7}Li solid-state MAS NMR spectra of *d*-LNMO and *o*-LNMO samples normalized to maximum intensity. Note that no additional peaks close to 0 ppm and associated with diamagnetic impurities are observed for *o*-LNMO in the full spectrum given in **Figure S9**, while there is a small diamagnetic signal for *d*-LNMO in relation with a tiny amount of residual LiCl precursor, not detected by XRD. For *o*-LNMO, one observes only signals in the 900-1000 ppm range, which agrees with the expected resonant shift for Li in a tetrahedral site in the $P4_332$ spinel structure and surrounded by 3 Ni^{2+} and 9 Mn^{4+} ions occupying the 4*b* and 12*d* sites,

respectively.[16,68] This result is in accordance with previously reported data for LNMO synthesized using a molten salt synthesis with an excess of salt.[52,69] Nevertheless, instead of observing a single resonance in this 900-1000 ppm region, the decomposition of the spectra of *o*-LNMO shows additional peaks with small shifts (~10-15 ppm) of different widths. These could be attributed to punctual Mn-Ni antisite defects, which do not modify the overall coordination sphere of lithium, keeping 9 Mn and 3 Ni atoms in its environment, but would slightly affect the local environment regarding the bond lengths and angles (see, for instance, ideal and O-Ni2Mn configurations in **Figure 6a**). In contrast, the NMR spectrum collected for *d*-LNMO shows a broader profile due to the co-existence of different Li environments, even if a dominant resonance is observed at around 920 ppm, like for *o*-LNMO. The decomposition of the spectrum reveals seven different contributions, which have been previously attributed to the wide distribution of Li environments where the Ni:Mn number of neighbors changes.[31,68,70] The line broadening can thus be explained by subtle differences regarding bond lengths and angles for a given Ni/Mn environment. Overall, these results indicate that the additional annealing step at 700°C for 24h under O_2 strongly orders *d*-LNMO in agreement with the previous trends reported on spinel structure.

The NMR shifts observed in paramagnetic compounds primarily arise from the delocalization of the unpaired *d* electrons of the transition metals to the probed nucleus, which induces a local magnetization known as the Fermi contact shift. The amount of transferred spin will depend on the local environment of the nucleus under measurement. Therefore, studying their local environments will sometimes help to get a rough understanding of changes in the NMR shifts. Nevertheless, even if estimations can sometimes be done depending on the nature, angle, and bond distances of the implied atoms, this is often much more complex, so for accurate results, DFT calculations are required. [26–29,71–75] In the spinel structure, lithium atoms lay in tetrahedral environments and are surrounded by four oxygen atoms. Each oxygen atom is at the same time linked to three additional transition metals (nickel or manganese). In the ordered $P4_332$ phase, there is ideally only a single lithium environment, as shown in **Figure 5a**. Each lithium is linked to 3 O-Mn_2Ni and to 1 O-Mn_3, making the first sphere of metal coordination of 9 Mn and 3 Ni. Therefore, even if there is a single lithium environment, there are two different oxygen environments. The spin transfer of the O-Mn_3 and O-Mn_2Ni configurations are shown in **Figures 5b** and **5c**, respectively. O-Mn_3 transfers a small positive spin (in yellow) to the lithium atom. In contrast, the positive spin transfer in O-Mn_2Ni is considerably larger; however, it does not directly point toward the lithium atom but in the opposite direction with respect to the nickel,

resulting in an angle of around 66° with the lithium atom. The sum of the spin transfers results in a calculated NMR shift of 940 ppm for the ordered structure according to DFT calculations, which strongly matches with the position of the experimental signal (920 ppm).

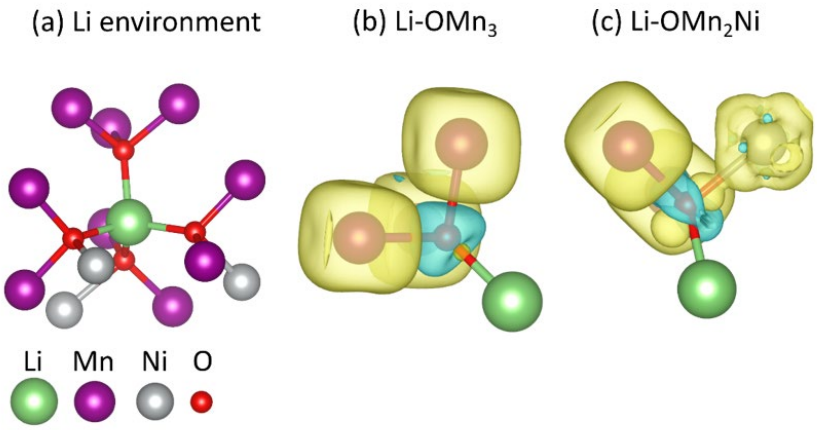

Figure 5: (a) Local environment around the lithium atom in the *o*-LNMO spinel. Spin density of the (b) O-Mn_3 and (c) O-Mn_2Ni configurations. For visualization purposes, only the spin density on the oxygen is shown, where the yellow density map represents the positive spin transfer, and the clear blue is the negative. Green spheres represent Li, purple spheres Mn, and grey spheres Ni.

The experimental ssNMR spectrum collected for *d*-LNMO typically exhibits multiple lithium environments (**Figure 4**). To correctly assign these environments, multiple LNMO structures have been generated by randomizing the positions of manganese and nickel atoms in the $Fd\bar{3}m$ cubic system with the help of the PyMatGen (Python Materials Genomics) library.[76] A total of 23 different possible configurations were considered, which have been named from S1 to S23, ordered according to their Ewald energy (the manganese has been treated as Mn^{4+} and the nickel as Ni^{2+}), S1 the most electrostatically stable and S23 the least (**Figure S10a**). The most stable first three structures contain an ordered arrangement, where all the lithium atoms are surrounded by 3 O-Mn_2Ni and 1 O-Mn_3. It is noticeable that the $P4_332$ (S3) is not the electrostatically most stable, and two more stable structures have been found. In contrast, in the rest of the computed structures, the disorder between transition metals is larger. The lower stability of the disordered phases is due to the local concentration of Mn^{4+}-rich and Ni^{2+}-rich clusters, resulting in irregular charge balance. For more accurate results, as well as the calculated NMR shift for each structure, DFT calculations have been carried out in the ten most electrostatically stable

structures (Figure S11), and their DFT energies are plotted in **Figure S10b**. In this case, the well-known ordered $P4_332$ (S3) is the most stable configuration after geometry optimization with DFT calculations. The second most stable structure, S2 shows an energy of 46 meV higher than S3. Even if the lithium atoms are also surrounded by 3 O-Mn_2Ni and 1 O-Mn_3 configurations, the relative positions of the transition metals result in different local geometry. Its computed NMR shift slightly varies from that observed for Li in the ideal $P4_332$ structure (960 ppm), which agrees with the interpretation we just proposed for the additional peaks observed in the spectrum of the *o*-LNMO. The rest of the considered structures have additional structural disorder, which generates different local environments for lithium versus the number of surrounding Ni and Mn ions. They are illustrated in **Figure 6a**, while their simulated NMR spectra based on calculated NMR shifts (**Table S7**) are displayed in **Figure 6b**.

Based on the computed NMR shifts, the resonances observed at 924 and 862 ppm for *d*-LNMO are both attributed to the ideal 1 O-Mn_3 and 3 O-Mn_2Ni configurations. The difference between these two chemical shifts comes from the second coordination environment; while the peak at 924 ppm comes from an ordered second coordination sphere, the resonance at 862 ppm is caused by a disordered second coordination sphere with manganese and/or nickel-rich zones. The resonance at 788 ppm is attributed to manganese-rich regions, where the first coordination sphere of lithium is composed of 10 Mn and 2 Ni atoms (2 O-Mn_3 and 2 O-Mn_2Ni). In contrast, when the coordination sphere of the lithium is nickel-rich with 8 Mn atoms and 4 nickel (4 O-Mn_2Ni), the NMR signal appears at higher ppm values than for the ideal environment. We can, therefore, conclude that the NMR spin density transfer of the O-Mn_3 is lower than the O-Mn_2Ni. Finally, we have also identified lithium atoms whose first coordination sphere is the same as the ideal one in terms of the number of atoms (9 Mn and 3 Ni), but their distribution among the oxygen atoms is different. In particular, one oxygen is linked to 2 nickel atoms forming a O-$MnNi_2$, and the rest of the environment is composed of 2 O-Mn_3 and 1 O-Mn_2Ni resulting in a chemical shift of 992 ppm. This study enables the accurate attribution, for the first time, of all the NMR signals observed for the disordered LNMO, demonstrating that the broad spectrum is not only observed due to differences in Mn:Ni ratio but can also arise from the different arrangements within the expected 3:1, and allowing for the quantification of each lithium environment. Finally, the additional experimental peaks observed at low ppm values (730 and 660 ppm) are assigned to Mn^{3+}-rich regions due to the higher presence of these found by the electrochemical analysis. However, in this work, only the stoichiometric formula has been considered.

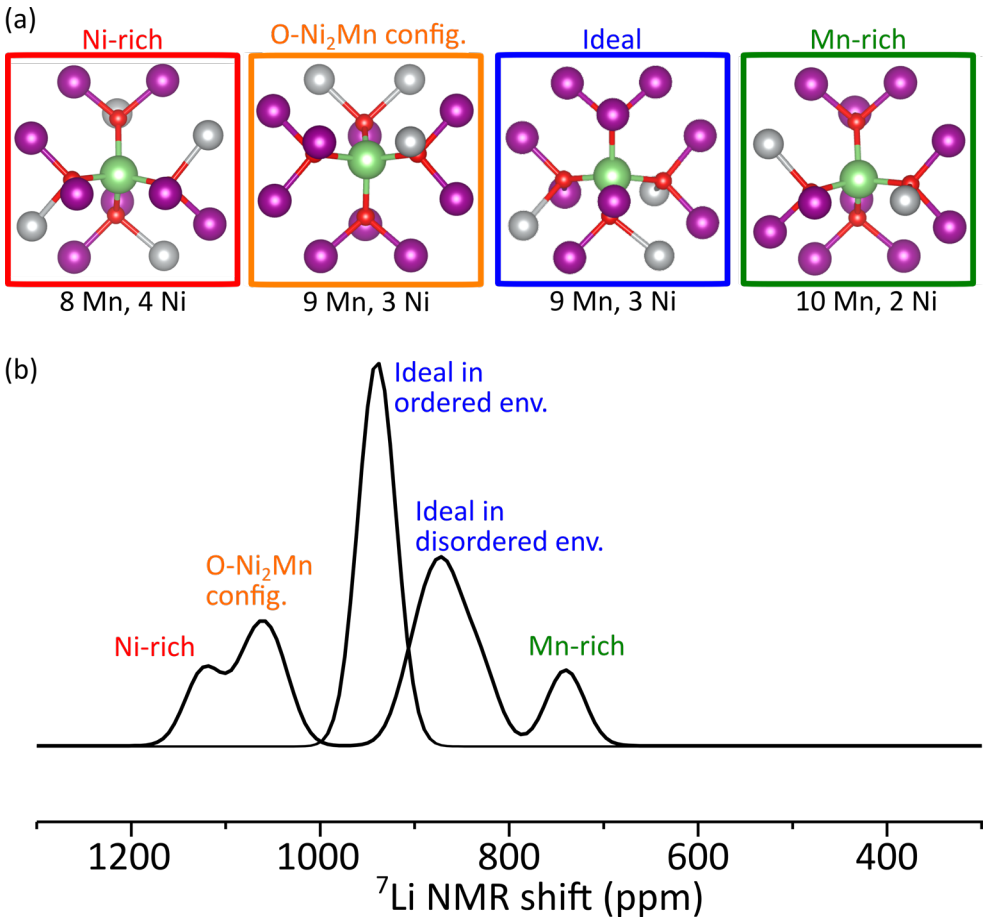

Figure 6: (a) Representation of Li configurations found in disordered spinel LNMO. Green, red, purple, and grey circles represent Li^{+}, O^{2-}, $Mn^{4+,}$ and Ni^{2+} ions. (b) Simulated NMR spectra for calculated structures containing the local environments shown in (a). The two ideal environments are different in their second coordination shells.

In summary, neutron diffraction refinements revealed that the spinel phase contained in *d*-LNMO has a Mn over-stoichiometry of 2.5 %, resulting in a Mn/Ni ratio of 1.54/0.46. Conversely, the spinel phase in *o*-LNMO was demonstrated to be close-to-ideal stoichiometry (*i.e.,* 1.5:0.5 for Mn:Ni) as expected for a fully ordered spinel. The compositions proposed for the spinel phases in both samples were supported by the redox processes involved upon cycling, showing the involvement of the Mn^{3+}/Mn^{4+} redox couple well aligned with the estimated contents in Mn^{3+}. Raman and NMR spectroscopies further confirmed the perfect ordering of o-LNMO from the long-range to the local scale with the support of theoretical calculations. For *d*-LNMO, the 160 cm^{-1} Raman vibration revealed limited coherent domain size, whereas NMR allowed the identification of a series of signals, some being associated with Mn-rich local

environments as expected by the over-stoichiometry in Mn. Note that Ni-rich local environments were also observed but in a much smaller amount, which is not enough for a composition compensation, suggesting that Ni-rich domains without Li exist.

Conclusions

The performance of the high voltage spinel $LiNi_{0.5}Mn_{1.5}O_4$ (LNMO) in Li-ion batteries strongly depends on its synthesis conditions, Ni/Mn stoichiometry, and degree of ordering of Ni and Mn. Depending on the extent of this ordering, the spinel structure can be described in the conventional space group $Fd\bar{3}m$ as the non-substituted $LiMn_2O_4$ or, for the highly ordered, in the space group $P4_332$. Two LNMO samples were prepared by molten salt syntheses using an excess of LiCl: disordered LNMO was obtained after annealing at 750°C under air, whereas the ordered LNMO was prepared from the first one with an additional annealing at 700°C under oxygen flow. The spinel phase composition was determined using neutron diffraction, showing an over-stoichiometry in Mn in good agreement with the content in Mn^{3+} estimated from the electrochemical mechanisms involved upon cycling. We have shown that Raman spectroscopy and especially the vibration band at ~160 cm^{-1} attributed for the first time, allows us to quantify roughly the degree of order/disorder in LNMO, whereas NMR spectroscopy allows us to give a clear description of the local environments of Li in LNMO. Theoretical calculations successfully supported the analysis and attribution of the Raman and NMR spectra/signals. These advanced characterizations enabled in-depth insights into the complexity of LNMO in stoichiometry, degree of ordering, and purity versus the presence of rock-salt or layered oxides as defects or crystalline domains. These findings promise to bring these Mn-rich high-voltage spinels, with controlled properties, as positive electrode materials into the next generation of Li-ion batteries.

Acknowledgments

The authors thank the Région Nouvelle Aquitaine and the ANR French National Research Agency (DESTINa-ion_Operando project ANR-19-CE42-0014-0202, VASELinNA project ANR-17-CE05-0010 and Labex STORE-EX project ANR-10-LABX-76-01) for their financial support. They also thank the ANR and Alistore-ERI for the funding of GO and JS's Ph.D. and postdoctoral fellowships, respectively. The Mésocentre de Calcul Intensif Aquitain (MCIA) and the modeling center of ISM are acknowledged for computing facilities. The authors are grateful to Emmanuel Petit, Catherine Denage, Jérôme Kalisky, Eric Lebraud, and Ilia Tertov at ICMCB for fruitful discussions and technical support.

References

1 G. Liang, V. K. Peterson, K. W. See, Z. Guo, and W. K. Pang, Developing high-voltage spinel $LiNi_{0.5}Mn_{1.5}O_4$ cathodes for high-energy-density lithium-ion batteries: current achievements and future prospects, *J. Mater. Chem. A*, 2020, **8**, 15373–15398.

2 M. Hu, X. Pang and Z. Zhou, Recent progress in high-voltage lithium ion batteries, *J. Power Sources*, 2013, **237**, 229–242.

3 X. Yu, W. A. Yu and A. Manthiram, Advances and Prospects of High-Voltage Spinel Cathodes for Lithium-Based Batteries, *Small Methods*, 2021, **2001196**, 1–30.

4 J. H. Kim, S. T. Myung, C. Yoon, S. G. Kang and Y. K. Sun, Comparative Study of $LiNi_{0.5}Mn_{1.5}O_{4-\delta}$ and $LiNi_{0.5}Mn_{1.5}O_4$ Cathodes Having Two Crystallographic Structures: Fd3m and $P4_332$, *Chem.Mater.*, 2004, **16**, 906–914.

5 J. Song, D. W. Shin, Y. Lu, C. D. Amos, A. Manthiram and J. B. Goodenough, Role of Oxygen Vacancies on the Performance of $Li[Ni_{0.5-x}Mn_{1.5+x}O_4$(x = 0, 0.05, and 0.08) Spinel Cathodes for Lithium-Ion Batteries, *Chem. Mater.*, 2012, **24**, 3101–3109.

6 B. Aktekin, M. Valvo, R. I. Smith, M. H. Sørby, F. Lodi Marzano, W. Zipprich, D. Brandell, K. Edström and W. R. Brant, Cation Ordering and Oxygen Release in $LiNi_{0.5-x}Mn_{1.5+x}O_{4-y}$ (LNMO): In Situ Neutron Diffraction and Performance in Li Ion Full Cells, *ACS Appl. Energy Mater.*, 2019, **2**, 3323–3335.

7 J. Cen, B. Zhu, S. R. Kavanagh, A. G. Squires and D. O. Scanlon, Cation disorder dominates the defect chemistry of high-voltage LiNi0.5Mn1.5O4 (LMNO) spinel cathodes, *J. Mater. Chem. A*, 2023, **11**, 13353–13370.

8 J. B. Goodenough and Y. Kim, Challenges for rechargeable Li batteries, *Chem. Mater.*, 2010, **22**, 587–603.

9 Y. Huang, Y. Dong, S. Li, J. Lee, C. Wang, Z. Zhu, W. Xue, Y. Li and J. Li, Lithium Manganese Spinel Cathodes for Lithium-Ion Batteries, *Adv. Energy Mater.*, 2021, **11**, 1–21.

10 J. H. Kim, A. Huq, M. Chi, N. P. W. Pieczonka, E. Lee, C. A. Bridges, M. M.

Tessema, A. Manthiram, K. A. Persson and B. R. Powell, Integrated nano-domains of disordered and ordered spinel phases in $LiNi_{0.5}Mn_{1.5}O_4$ for li-ion batteries, *Chem. Mater.*, 2014, **26**, 4377–4386.

11 M. Casas-Cabanas, C. Kim, J. Rodríguez-Carvajal and J. Cabana, Atomic defects during ordering transitions in $LiNi_{0.5}Mn_{1.5}O_4$ and their relationship with electrochemical properties, *J. Mater. Chem. A*, 2016, **4**, 8255–8262.

12 N. Emery, A. Bhatia, Y. Ghaleb, A. O. Mitrushchenkov, C. Léonard, J.-P. Pereira-Ramos, R. Baddour-Hadjean and R. I. Smith, Short-Range to Long-Range Ni/Mn Order in $LiMn_{2-x}Ni_xO_4$ ($0.38 \leq x \leq 0.50$) Positive Electrode Materials: A Gradual Temperature-Driven Sublattice Disorder through Antiphase Boundary Defects, *Chem. Mater.*, 2022, **34**, 3152–3167.

13 L. Cai, Z. Liu, K. An and C. Liang, Unraveling structural evolution of $LiNi_{0.5}Mn_{1.5}O_4$ by in situ neutron diffraction, *J. Mater. Chem. A*, 2013, **1**, 6908–6914.

14 Y. Chen and K. An, Unraveling transition-metal-mediated stability of spinel oxide via in situ neutron scattering, *J. Energy Chem.*, 2022, **68**, 60–70.

15 D. W. Shin, C. A. Bridges, A. Huq, M. P. Paranthaman and A. Manthiram, Role of Cation Ordering and Surface Segregation in High-Voltage Spinel $LiMn_{1.5}Ni_{0.5-x}M_xO_4$ (M = Cr, Fe, and Ga) Cathodes for Lithium-Ion Batteries, *Chem. Mater.*, 2012, **24**, 3720–3731.

16 C. P. Grey and Y. J. Lee, Lithium MAS NMR studies of cathode materials for lithium-ion batteries, *Solid State Sci.*, 2003, **5**, 883–894.

17 X. Liu, Z. Liang, Y. Xiang, M. Lin, Q. Li, Z. Liu, G. Zhong, R. Fu and Y. Yang, Solid-State NMR and MRI Spectroscopy for Li/Na Batteries: Materials, Interface, and In Situ Characterization, *Adv. Mater.*, 2021, **33**, 1–21.

18 P. B. Samarasingha, N. H. Andersen, M. H. Sørby, S. Kumar, O. Nilsen and H. Fjellvåg, Neutron diffraction and Raman analysis of $LiNi_{0.5}Mn_{1.5}O_4$spinel type oxides for use as lithium ion battery cathode and their capacity enhancements, *Solid State Ionics*, 2016, **284**, 28–36.

19 A. Bhatia, Y. Dridi Zrelli, J.-P. Pereira-Ramos and R. Baddour-Hadjean, Detailed redox mechanism and self-discharge diagnostic of 4.9 V $LiNi_{0.5}Mn_{1.5}O_4$ spinel cathode revealed by Raman spectroscopy, *J. Mater. Chem. A*, , DOI:10.1039/d1ta00989c.

20 J. Yoon, D. Kim, J. H. Um, M. Jeong, W. Oh and W. S. Yoon, Effect of local structural changes on rate capability of $LiNi_{0.5}Mn_{1.5}O_{4-\delta}$ cathode material for lithium ion batteries, *J. Alloys Compd.*, 2016, **686**, 593–600.

21 K. Ariyoshi, Y. Iwakoshi, N. Nakayama and T. Ohzuku, Topotactic Two-Phase Reactions of $Li[Ni_{1/2}Mn_{3/2}]O_4$ ($P4_332$) in Nonaqueous Lithium Cells, *J. Electrochem. Soc.*, 2004, **151**, A296–A303.

22 L. Boulet-Roblin, C. Villevieille, P. Borel, C. Tessier, P. Novák and M. Ben Yahia, Versatile approach combining theoretical and experimental aspects of Raman spectroscopy to investigate battery materials: The case of the $LiNi_{0.5}Mn_{1.5}O_4$ spinel, *J. Phys. Chem. C*, 2016, **120**, 16377–16382.

23 K. Miwa, Prediction of Raman spectra with DFT+ U method, *Phys. Rev. B*, 2018, **97**, 1–7.

24 H. Liu, X. Zhang, X. He, A. Senyshyn, A. Wilken, D. Zhou, O. Fromm, P. Niehoff, B. Yan, J. Li, M. Muehlbauer, J. Wang, G. Schumacher, E. Paillard, M. Winter and J. Li, Truncated Octahedral High-Voltage Spinel $LiNi_{0.5}Mn_{1.5}O_4$ Cathode Materials for Lithium Ion Batteries: Positive Influences of Ni/Mn Disordering and Oxygen Vacancies, *J. Electrochem. Soc.*, 2018, **165**, A1886–A1896.

25 P. Stüble, V. Mereacre, H. Geßwein and J. R. Binder, On the Composition of $LiNi_{0.5}Mn_{1.5}O_4$ Cathode Active Materials, *Adv. Energy Mater.*, 2023, **13**, 2203778.

26 D. Carlier, M. Ménétrier, C. P. Grey, C. Delmas and G. Ceder, Understanding the NMR shifts in paramagnetic transition metal oxides using density functional theory calculations, *Phys. Rev. B - Condens. Matter Mater. Phys.*, 2003, **67**, 1–14.

27 J. Serrano-Sevillano, D. Carlier, A. Saracibar, J. M. Lopez Del Amo and M. Casas-Cabanas, DFT-Assisted Solid-State NMR Characterization of Defects in Li_2MnO_3, *Inorg. Chem.*, 2019, **58**, 8347–8356.

28 W. S. Yoon, S. Iannopollo, C. P. Grey, D. Carlier, J. Gorman, J. Reed and G. Ceder, Local structure and cation ordering in O3 lithium nickel manganese oxides with stoichiometry $Li[Ni_xMn_{(2-x)/3}Li_{(1-2x)/3}]$ O_2 NMR studies and first principles calculations, *Electrochem. Solid-State Lett.*, 2004, **7**, 3–8.

29 L. H. B. Nguyen, P. Sanz Camacho, T. Broux, J. Olchowka, C. Masquelier, L. Croguennec and D. Carlier, Density Functional Theory-Assisted ^{31}P and ^{23}Na Magic-Angle Spinning Nuclear Magnetic Resonance Study of the $Na_3V_2(PO_4)_2F_3$–$Na_3V_2(PO_4)$₂, *Chem. Mater.*, 2019, **31**, 9759–9768.

30 Y. J. Lee and C. P. Grey, Determining the lithium local environments in the lithium manganates $LiZn_{0.5}Mn_{1.5}O_4$ and Li_2MnO_3 by analysis of the ^6Li MAS NMR spinning sideband manifolds, *J. Phys. Chem. B*, 2002, **106**, 3576–3582.

31 J. Cabana, M. Casas-Cabanas, F. O. Omenya, N. A. Chernova, D. Zeng, M. S. Whittingham and C. P. Grey, Composition-Structure Relationships in the Li-Ion Battery Electrode Material $LiNi_{0.5}Mn_{1.5}O_4$, *Chem. Mater.*, 2012, **24**, 2952–2964.

32 G. Oney, J. Olchowka, A. Demortière, F. Weill and L. Croguennec, Molten Salt Synthesis of Multifaceted Pure-Phase Spinel $LiNi_{0.5}Mn_{1.5}O_4$ Platelets, *ACS Appl. Energy Mater.*, 2023, **6**, 8189–8196.

33 J. Rodríguez-Carvajal, Recent advances in magnetic structure determination by neutron powder diffraction, *Phys. B*, 1993, **192**, 55–69.

34 D. Massiot, F. Fayon, M. Capron, I. King, S. Le Calvé, B. Alonso, J. O. Durand, B. Bujoli, Z. Gan and G. Hoatson, Modelling one- and two-dimensional solid-state NMR spectra, *Magn. Reson. Chem.*, 2002, **40**, 70–76.

35 A. D. Becke, A new mixing of Hartree-Fock and local density-functional theories, *J. Chem. Phys.*, 1993, **98**, 1372–1377.

36 R. Dovesi, F. Pascale, B. Civalleri, K. Doll, N. M. Harrison, I. Bush, P. D'Arco, Y. Noel, M. Rera, P. Carbonniere, M. Causa, S. Salustro, V. Lacivita, B. Kirtman, A. M. Ferrari, F. S. Gentile, J. Baima, M. Ferrero, R. Demichelis and M. De La Pierre, The CRYSTAL code, 1976-2020 and beyond, a long story, *J. Chem. Phys.*, , DOI:10.1063/5.0004892.

37 L. De Pe and P. Jussieu, The Calculation of the Vibrational Frequencies of, *J. Comput.*

Chem., 2004, 888–897.

38 L. Ojamäe, K. Hermansson, C. Pisani, M. Causà and C. Roetti, Structural, vibrational and electronic properties of a crystalline hydrate from ab initio periodic Hartree–Fock calculations, *Acta Crystallogr. Sect. B*, 1994, **50**, 268–279.

39 M. Ben Yahia, F. Lemoigno, T. Beuvier, J. Ś. Filhol, M. Richard-Plouet, L. Brohan and M. L. Doublet, Updated references for the structural, electronic, and vibrational properties of TiO_2 (B) bulk using first-principles density functional theory calculations, *J. Chem. Phys.*, , DOI:10.1063/1.3130674.

40 R. Dovesi, A. Erba, R. Orlando, C. M. Zicovich-Wilson, B. Civalleri, L. Maschio, M. Rérat, S. Casassa, J. Baima, S. Salustro and B. Kirtman, Quantum-mechanical condensed matter simulations with CRYSTAL, *Wiley Interdiscip. Rev. Comput. Mol. Sci.*, 2018, **8**, 1–36.

41 M. Ferrero, M. Rérat, R. Orlando and R. Dovesi, The Calculation of Static Polarizabilities of 1-3D Periodic Compounds. The Implementation in the CRYSTAL Code, *J. Comput. Chem.*, 2008, **29**, 1450–1459.

42 L. Maschio, B. Kirtman, M. Rérat, R. Orlando and R. Dovesi, Ab initio analytical Raman intensities for periodic systems through a coupled perturbed Hartree-Fock/Kohn-Sham method in an atomic orbital basis. I. Theory, *J. Chem. Phys.*, , DOI:10.1063/1.4824442.

43 M. D. Towler, N. L. Allan, N. M. Harrison, V. R. Saunders, W. C. MacKrodt and E. Aprà, Ab initio study of MnO and NiO, *Phys. Rev. B*, 1994, **50**, 5041–5054.

44 G. Kresse and J. Furthmüller, Efficiency of ab-initio total energy calculations for metals and semiconductors using a plane-wave basis set, *Comput. Mater. Sci.*, 1996, **6**, 15–50.

45 D. Joubert, From ultrasoft pseudopotentials to the projector augmented-wave method, *Phys. Rev. B - Condens. Matter Mater. Phys.*, 1999, **59**, 1758–1775.

46 J. P. Perdew, K. Burke and M. Ernzerhof, Generalized gradient approximation made simple, *Phys. Rev. Lett.*, 1996, **77**, 3865–3868.

47 S. L. Dudarev, G. A. Botton, S. Y. Savrasov, Z. Szotek, W. M. Temmerman and A. P. Sutton, Electronic structure and elastic properties of strongly correlated metal oxides from first principles: LSD A + U, SIC-LSDA and EELS study of UO_2 and NiO, *Phys. Status Solidi Appl. Res.*, 1998, **166**, 429–443.

48 L. H. B. Nguyen, A. Iadecola, S. Belin, J. Olchowka, C. Masquelier, D. Carlier and L. Croguennec, A combined operando synchrotron x-ray absorption spectroscopy and first-principles density functional theory study to unravel the vanadium redox paradox in the Na3V2(PO4)2F3</sub>−$Na_3V_2(PO_4)_2FO_2$ compo, *J. Phys. Chem. C*, 2020, **124**, 23511–23522.

49 T. Bamine, E. Boivin, F. Boucher, R. J. Messinger, E. Salager, M. Deschamps, C. Masquelier, L. Croguennec, M. Ménétrier and D. Carlier, Understanding Local Defects in Li-Ion Battery Electrodes through Combined DFT/NMR Studies: Application to $LiVPO_4F$, *J. Phys. Chem. C*, 2017, **121**, 3219–3227.

50 T. Bamine, E. Boivin, C. Masquelier, L. Croguennec, E. Salager and D. Carlier, Local atomic and electronic structure in the $LiVPO_4(F,O)$ tavorite-type materials from solid-

state NMR combined with DFT calculations, *Magn. Reson. Chem.*, 2020, **58**, 1109–1117.

51 Y. Qian, Y. Deng, L. Wan, H. Xu, X. Qin and G. Chen, Investigation of the Effect of Extra Lithium Addition and Postannealing on the Electrochemical Performance of High-Voltage Spinel $LiNi_{0.5}Mn_{1.5}O_4$ Cathode Material, *J. Phys. Chem. C*, 2014, **118**, 15581–15589.

52 H. Duncan, B. Hai, M. Leskes, C. P. Grey and G. Chen, Relationships between Mn^{3+} Content, Structural ordering, Phase transformation, and Kinetic Properties in $LiNi_xMn_{2-x}O_4$ Cathode Materials, *Chem. Mater.*, 2014, **26**, 5374–5382.

53 D. C. Peaslee, Neutron scattering lengths, *Phys. Rev.*, 1952, **85**, 555–558.

54 Z. Tong, Q. Ye, Y. Deng, Q. She, A. Huang, J. Xu and X. Zhu, Tuning the structural disordering in hierarchical $LiNi_{0.5}Mn_{1.5}O_4$ microrods for stable high-rate electrode performance, *J. Alloys Compd.*, 2023, **937**, 168544.

55 L. Wang, H. Li, X. Huang and E. Baudrin, A comparative study of Fd-3m and $P4_332$' $LiNi_{0.5}Mn_{1.5}O_4$', *Solid State Ionics*, 2011, **193**, 32–38.

56 C. M. Julien, F. Gendron, A. Amdouni and M. Massot, Lattice vibrations of materials for lithium rechargeable batteries. VI: Ordered spinels, *Mater. Sci. Eng. B*, 2006, **130**, 41–48.

57 A. Falcone, Université de Montpellier, 2021.

58 B. Rivas-Murias and V. Salgueiriño, Thermodynamic CoO–Co_3O_4 crossover using Raman spectroscopy in magnetic octahedron-shaped nanocrystals, *J. Raman Spectrosc.*, 2017, **48**, 837–841.

59 X. Cai, W. Sun, C. Xu, L. Cao and J. Yang, Highly selective catalytic reduction of NO via SO_2/H_2O-tolerant spinel catalysts at low temperature, *Environ. Sci. Pollut. Res.*, 2016, **23**, 18609–18620.

60 Z. Ž. Lazarević, Č. Jovalekić, D. Sekulić, M. Slankamenac, M. Romčević, A. Milutinović and N. Ž. Romčević, Characterization of nanostructured spinel $NiFe_2O_4$ obtained by soft mechanochemical synthesis, *Sci. Sinter.*, 2012, **44**, 331–339.

61 Z. Ž. Lazarević, Č. Jovalekić, A. Milutinović, D. Sekulić, M. Slankamenac, M. Romčević and N. Ž. Romčević, Study of $NiFe_2O_4$ and $ZnFe_2O_4$ Spinel Ferrites Prepared by Soft Mechanochemical Synthesis, *Ferroelectrics*, 2013, **448**, 1–11.

62 Editor: Russell D. Johnson III, Release 22.

63 H. Richter, Z. P. Wang and L. Ley, The one phonon Raman spectrum in microcrystalline silicon, *Solid State Commun.*, 1981, **39**, 625–629.

64 V. I. Korepanov, S. Y. Chan, H. C. Hsu and H. o. Hamaguchi, Phonon confinement and size effect in Raman spectra of ZnO nanoparticles, *Heliyon*, 2019, **5**, 1–14.

65 M. Tanwar, P. Yogi, S. Lambora, S. Mishra, S. K. Saxena, P. R. Sagdeo, A. S. Krylov and R. Kumar, Generalisation of phonon confinement model for interpretation of Raman line-shape from nano-silicon, *Adv. Mater. Process. Technol.*, 2018, **4**, 227–233.

66 Loridant S., *Characterization of Nanomaterials*, Woodhead Publishing, 2018.

67 J. Bréger, M. Jiang, N. Dupré, Y. S. Meng, Y. Shao-Horn, G. Ceder and C. P. Grey, High-resolution X-ray diffraction, DIFFaX, NMR and first principles study of disorder in the Li_2MnO_3-$Li[Ni_{1/2}Mn_{1/2}]O_2$ solid solution, *J. Solid State Chem.*, 2005, **178**, 2575–2585.

68 J. Lee, N. Dupre, M. Avdeev and B. Kang, Understanding the cation ordering transition in high-voltage spinel $LiNi_{0.5}Mn_{1.5}O_4$ by doping Li instead of Ni, *Sci. Rep.*, 2017, **7**, 1–12.

69 B. Hai, A. K. Shukla, H. Duncan and G. Chen, The effect of particle surface facets on the kinetic properties of $LiNi_{0.5}Mn_{1.5}O_4$ cathode materials, *J. Mater. Chem. A*, 2013, **1**, 759–769.

70 Y. J. Lee, C. Eng and C. P. Grey, ^{6}Li Magic Angle Spinning NMR Study of the Cathode Material $LiNi_xMn_{2-x}O_4$: The Effect of Ni Doping on the Local Structure during Charging, *J. Electrochem. Soc.*, 2001, **148**, A249.

71 Y. Zhang, A. Castets, D. Carlier, M. Ménétrier and F. Boucher, Simulation of NMR Fermi contact shifts for lithium battery materials: The need for an efficient hybrid functional approach, *J. Phys. Chem. C*, 2012, **116**, 17393–17402.

72 P. C. M. M. Magusin, I. D. Seymour, O. Pecher and C. P. Grey, in *Modern Methods in Solid-state NMR: A Practitioner's Guide*, ed. P. Hodgkinson, The Royal Society of Chemistry, 2018, pp. 322–55.

73 R. J. Clément, A. J. Pell, D. S. Middlemiss, F. C. Strobridge, J. K. Miller, M. S. Whittingham, L. Emsley, C. P. Grey and G. Pintacuda, Spin-Transfer Pathways in Paramagnetic Lithium Transition-Metal Phosphates from Combined Broadband Isotropic Solid-State MAS NMR spectroscopy and DFT Calculations, *J. Am. Chem. Soc.*, 2012, **134**, 17178–17185.

74 A. Castets, D. Carlier, Y. Zhang, F. Boucher, N. Marx, L. Croguennec and M. Ménétrier, Multinuclear NMR and DFT Calculations on the $LiFePO_4$·OH and $FePO_4$·H_2O Homeotypic Phases, *J. Phys. Chem. C*, 2011, **115**, 16234–16241.

75 J. Kim, D. S. Middlemiss, N. A. Chernova, B. Y. X. Zhu, C. Masquelier and C. P. Grey, Linking Local Environments and Hyperfine Shifts: A Combined Experimental and Theoretical ^{31}P and ^{7}Li Solid-State NMR Study of Paramagnetic Fe(III) Phosphates, *J. Am. Chem. Soc.*, 2010, **132**, 16825–16840.

76 S. P. Ong, W. D. Richards, A. Jain, G. Hautier, M. Kocher, S. Cholia, D. Gunter, V. L. Chevrier, K. A. Persson and G. Ceder, Python Materials Genomics (pymatgen): A robust, open-source python library for materials analysis, *Comput. Mater. Sci.*, 2013, **68**, 314–319.